Behavior of Sputtered Tungsten in the Divertor Plasma Simulator NAGDIS-II

Hirohiko TANAKA[1,2)]*, Shin KAJITA[2,3)], Noriyasu OHNO[1,2)]

[1)] Institute of Materials and Systems for Sustainability, Nagoya University, Furo-cho, Chikusa-ku, Nagoya 464-8603, Japan
[2)] Graduate School of Engineering, Nagoya University, Furo-cho, Chikusa-ku, Nagoya 464-8603, Japan
[3)] Graduate School of Frontier Sciences, The University of Tokyo, Kashiwa, Chiba 277-8561, Japan

(Received 28 October 2024 / Accepted 21 January 2025)

The core-degradation effect due to tungsten (W) - a proposed plasma-facing material for the operation of future nuclear fusion reactors such as ITER and DEMO - calls for the study of sputtered W. In this study, sputtered W from a point source in the linear divertor plasma simulator, NAGDIS-II, was investigated. A hyperspectral imaging (HSI) camera was used to image the spatial profile of the sputtered W in helium and argon mixture plasma with different incident ion energies. By applying the Abel transform and fittings with several functions and comparing with the theoretical value, it is found that the ionization effect is not obvious but the geometrical spreading effect is dominant for the axial decay of the local W emission profile.

Keywords: tungsten sputtering, decay length, hyperspectral imaging, divertor plasma simulator, NAGDIS-II

DOI: 10.1585/pfr.20.1302020

The plasma-facing components (PFCs) in fusion reactors must meet very complex and stringent requirements. The PFCs are exposed to high heat flux from the plasma. In addition, high-energy ions including impurity heavy ions, which are injected in to cool the plasma, are accelerated by the electric sheath and exposed to the surface of PFCs, resulting in the erosion and also the re-deposition [1, 2]. Tungsten (W) is chosen as the material for PFCs in fusion reactors due to its high melting point, low tritium retention, and low sputtering yield [3–5]. However, tungsten with high-Z significantly deteriorates the core plasma performance due to the strong radiation, as it has a lower acceptable impurity concentration [6, 7].

There are several ambiguities in assessing the effect of W impurity. One is in the erosion rate. The sputtering yield can be significantly changed because the surface morphology is altered by the plasma bombardment [8–10]. In addition to the steady state load, the erosion in response to transients accompanied by edge localized mode (ELM) is an important issue because it can cause the melting of W material [11] and the ignition of unipolar arcs [12, 13]. It is also important to understand the effect of W after sputtering [14]. JET ITER-like wall experiments have shown that the application of ion cyclotron radio frequency heating at the very center of the plasma contributed to a significantly lower central tungsten peaking [15]. Recently, using a collisional-radiative model, it has been discussed that the effect of the magnetic presheath is important to consider the W migration [16]. Although the control of the W transport in the plasma is important, it is not yet fully understood.

Tungsten co-deposition experiments have been performed in linear divertor plasma simulators such as Magnum-PSI, NAGDIS-II, Co-NAGDIS, and PISCES-RF [17–20]. The elucidation of the sputtered W behavior is important to understand the deposition-induced morphology changes, such as the enhanced growth process of tungsten nanostructures (fuzz) [10], as well as the highly porous co-deposition layer, whose properties are quite different from those of the bulk material. In this study, the sputtered W behavior is studied in the linear divertor simulator NAGDIS-II. The emission profile was recorded using a hyperspectral imaging camera. These emission profiles are then analyzed to deduce the axial decay length of sputtered W atoms after the Abel transform to eliminate the line integral effect. Based on the experimental results and the theoretical calculation, the physical processes that determine the decay length will be discussed.

The linear divertor plasma simulator NAGDIS-II [21] was used in this experimental study, where steady-state plasma with the electron density (n_e) up to 10^{20} m^{-3} can be generated. Figure 1 shows a side view and a front view of the schematic of the plasma column with the irradiation experiment setup performed in the midstream region of NAGDIS-II. In this experiment, helium (He) gas is introduced from the upstream side of the device for plasma discharge, while argon (Ar) gas is introduced from the downstream side for enhancing the sputtering process and simulating the impurity seeding. Thus, a mixed He-Ar plasma is generated. The discharge current, discharge voltage, and magnetic field strength are 20 A, 120 V and 0.1 T, respectively. The total neutral

*Corresponding author's e-mail: h-tanaka@ees.nagoya-u.ac.jp

pressure measured with a capacitance manometer is 8.8 mTorr, and the partial pressure of Ar is 5.4 mTorr. The typical plasma diameter is ~ 20 mm, and the plasma parameters measured by a Langmuir probe at the center of the plasma column are the electron temperature (T_e) of 4 eV, the electron density (n_e) of 1 × 10^{18} m^{-3}, and the space potential of −5 eV. As described later, an existence of Ar ions is confirmed by the spectroscopy, although its density has not been estimated. A certain amount of Ar ions would be present, as the ionization rate coefficient is ~ 78 times higher than helium at T_e = 4 eV [22].

To prepare a local sputtering source for the Abel transform described later, a small W disc with a diameter of ~ 3 mm and a thickness of 0.5 mm is inserted into the plasma column. The W sample is held by a wire covered with a ceramic (Al_2O_3) insulating tube. The normal direction of the W surface is parallel to the magnetic field. The W sample is negatively biased at −100, −150, −200, −250, or −300 V from the ground potential. The incident ion energy, E_0, on the sample was a difference between the space potential and the potential of the sample. Now that the space potential is so small (~ −5 V), E_0 is almost equal to the absolute value of the bias voltage as E_0 ~ 100, 150, 200, 250, or 300 V. Since the sputtering yield of W by Ar is much higher than that by He (~ 40 times higher at E_0 = 300 eV [23]), a number of W particles are sputtered by Ar and ejected into the plasma.

A hyperspectral imaging (HSI) camera (Spectral Imaging, Specim IQ) was used to capture the spatial profile of the W emission from the sputtered W particles. The HSI camera observed the plasma column through a viewing window. A schematic of the field of view (FOV) is shown in Fig. 1. The right side is upstream (discharge region) and the left side is downstream (end target). In this imaging technique, information is collected as a set of images, a three-dimensional (x, y, λ) data cube, where x and y are the horizontal and vertical positions and λ is the wavelength. The same type of HSI camera was also used in the previous research performed in another linear plasma device PISCES-A to measure the chromium emission in He plasma [24]. The measurement wavelength range is 400–1,000 nm and the spectral resolution (FWHM) is 7 nm. The pixel resolution is ~ 0.5 mm/pixel. In addition, a compact spectrometer (AVANTES, AvaSpec-ULS3648) is used to identify the emission lines with a higher wavelength resolution of 0.3–0.4 nm, which is much smaller than that of the HSI camera (7 nm). The compact spectrometer is placed at the same position as the HSI camera, and the line-integrated emission was captured near the W sample through a collimating lens.

Figure 2(a) shows typical emission spectra obtained from the HSI camera and the compact spectrometer. Here, the compact spectrometer result shows two cases: with (−300 V) and without biasing (floating) the W disc. Several line emissions from He and Ar can be identified under the floating condition, *e.g.*, 402.6 and 447.2 nm for He I, 415.9 nm for Ar I and 434.8 nm for Ar II. The Ar II emission is from Ar ions. In addition to this, a number of W lines are seen with the negative bias, *e.g.*, 400.9, 404.6, 407.4, 424.4, 426.9, 429.5, and 430.2 nm for W I. Due to the lower resolution of the HSI camera, multiple line emissions are merged into a single peak at ~ 429 nm. In Fig. 2(b), we compared the peak intensities measured with the HSI camera at ~ 429 nm and compact spectrometer at 429.5 nm (W I line) with several bias cases. A linear relationship is observed, indicating that the HSI camera mainly captures the W I emission. In the following, 2D HSI camera data at ~ 429 nm will be used to observe the 2D distribution of W I emission.

Figure 3(a) shows the 2D image of the sputtered W emission near the W disc after subtracting the background. The background was calculated by averaging the tail ends of

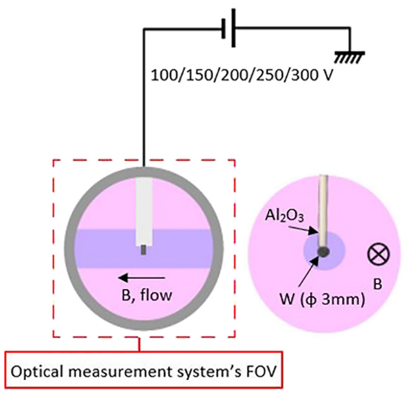

Fig. 1. A schematic of the experimental setup of He-Ar mixture plasma irradiation in the NAGDIS-II viewed from the side (left) and from the front inside the device (right).

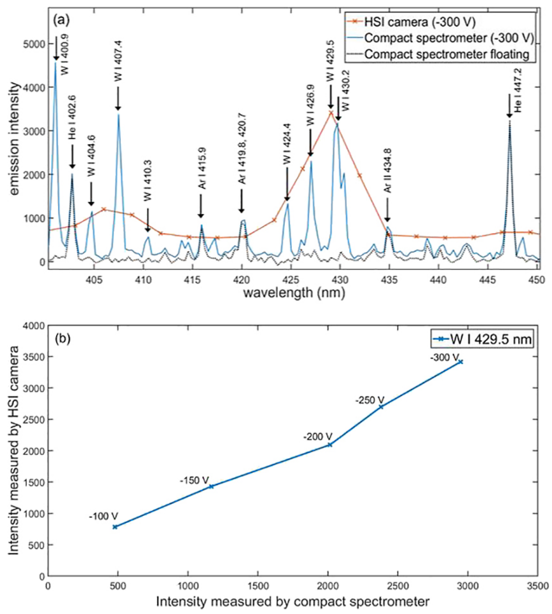

Fig. 2. (a) Typical emission spectra measured with the HSI camera with −300 V bias (red line) and the compact spectrometer with −300 V bias (blue line) and in floating condition (black dotted line). (b) W I (429.46 nm) line's intensity measured in both the HSI camera and the compact spectrometer for different applied biases.

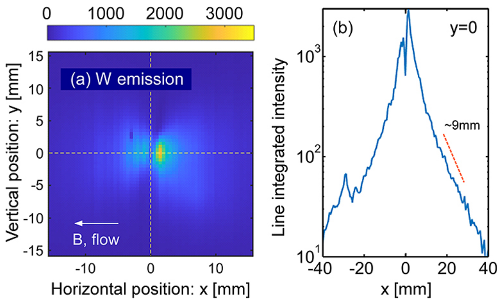

Fig. 3. (a) 2D image and (b) horizontal slice at $y = 0$ of the W emission profile obtained from the HSI camera for −300 V at 10 ms integration time.

the spectral peak along the wavelength ([416, 419] nm and [439, 442] nm). At the W disc location at $(x, y) \sim (0, 0)$, there is a dip in the emission, because of existences of the W disc and the electric sheath. In addition, stronger W emission is seen on the right hand side, which points to the upstream region where higher density plasma exists. Figure 3(b) shows the horizontal slice of Fig. 3(a) at $y = 0$. At $x \sim 20$ mm, the exponential decay length is about 9 mm but it includes the line integral and the geometric effect as described below.

In the following, the decay length of the W emission intensity will be examined from local values converted using Abel transform. For the application of Abel transform, it was assumed that the W emission was symmetrical about the central axis of the plasma column and W disc. Because of the disturbance to the W emission caused by the ceramic tube at upper region ($y > 0$), only the lower part ($y \leq 0$) was analyzed at each horizontal position. The axial profiles of W emission intensity after performing the Abel transform for all differently biased conditions (i.e., −100, −150, −200, −250, and −300 V) are shown in Fig. 4(a). As these are local values on the axis, the shape of the profile does not include the effect of the incident energy dependence of the emitting angle of the sputtered particles [25]. For each profile, the emission intensity decreases monotonically with distance. With increasing the absolute value of the disc biasing, the emission intensity increases and long tail component gradually appears. The intensity drops sharply upto $\sim$ 10 mm, and decrease slowly at > 10 mm.

When the decay process of the local emission $I_{\mathrm{local}}(x)$ along the axis is determined only by extinction processes such as electron impact ionization, the emission can be described by an exponential function [26] as

$$I_{\mathrm{local}}(x) \propto \exp\left[-(x - x_{\mathrm{W}})/\lambda_{\mathrm{W}}\right], \tag{1}$$

where λ_{W} is the mean free path. However, the decay cannot be simply explained by Eq. (1) as shown in Fig. 4(b), which is the magnified view at $x \geq 0$ for −300 V bias. Here, the exponential curve (orange dashed line) in this diagram has λ_{W} of $\sim$ 6 mm. Other effects should be considered and are discussed in the next part.

The theoretical decay length (mean free path) of a sputtered tungsten atom by Ar ions is calculated considering electron-impact ionization. The equation to calculate the mean

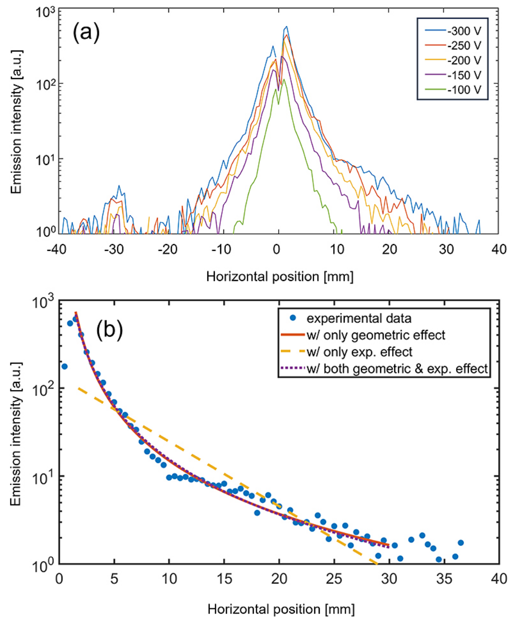

Fig. 4. (a) Abel-transformed emission intensities along the axis for different applied biases. (b) Magnified view of the Abel-transformed emission intensity at $x \geq 0$ for −300 V bias with three different fittings (Eqs. (2) with red solid line, (1) with orange dashed line, and (3) with purple dotted line).

Table 1. Sputtered energy coefficient $Y_{\mathrm{E}}(E_0)$, sputtering yield $Y(E_0)$, and calculated mean free path λ_{m} of W due to the ionization when Ar particles impact with different incident ion energies (E_0 = 100, 200, and 300 eV).

E_0 [eV]	$Y_{\mathrm{E}}(E_0)$	$Y(E_0)$	λ_{m} [mm]
100	4.45×10^{-3}	5.60×10^{-2}	79.3
200	1.35×10^{-2}	2.01×10^{-1}	103
300	1.88×10^{-2}	3.36×10^{-1}	115

free path is given as $\lambda_{\mathrm{m}} = v_{\mathrm{W}}/n_{\mathrm{e}}\langle\sigma_{\mathrm{ion}}v_{\mathrm{e}}\rangle$, where v_{W} is the speed of sputtered tungsten atoms, and $\langle\sigma_{\mathrm{ion}}v_{\mathrm{e}}\rangle$ is the ionization rate, which is $\sim 3.63 \times 10^{-14}$ m^3/s at $T_{\mathrm{e}} = 4$ eV in OPEN-ADAS [27]. Here, v_{W} can be determined from the average energy of sputtered atoms $\langle E(E_0)\rangle$ due to incident ion energy E_0 and mass of tungsten atom m_{W} through the relation as $v_{\mathrm{W}} = \sqrt{2\langle E(E_0)\rangle/m_{\mathrm{W}}}$. The average energy of sputtered atoms $\langle E(E_0)\rangle$ can be calculated from the relation $\langle E(E_0)\rangle = (E_0 Y_{\mathrm{E}}(E_0))/(Y(E_0))$, where $E_0 Y_{\mathrm{E}}(E_0)$ is the sputtered energy of W by Ar and $Y(E_0)$ is the sputtering yield of W by Ar in the normal direction [23]. The calculated theoretical decay length for different scenarios carried out in experiments is given in the Table 1. It is seen that the mean free path exceeds 100 mm when $E_0 \geq 200$ V, which is much longer than the typical decay length in Fig. 4(b).

In the present experiments, because the W particles are released from the small W disc, it is necessary to consider the geometrical spreading effect. Since W particles emitted in a certain solid angle spread over an area that is proportional to the square of the distance, particle number on the axis will be as follows:

$$I_{\mathrm{local}}(x) \propto (x - x_{\mathrm{W}})^{-2}, \quad (2)$$

where x_{W} is the W source position and it could shift from the actual position when the fitting because the W source has a finite size. Furthermore, by considering the ionization process, the local emission along the axis would be expressed as

$$I_{\mathrm{local}}(x) \propto (x - x_{\mathrm{W}})^{-2} \cdot \exp\ [-(x - x_{\mathrm{W}})/\lambda_{\mathrm{W}}]. \quad (3)$$

Figure 4(b) shows the fitting curves with Eqs. (2) and (3). These fittings are almost identical, meaning that the exponential-decay term is negligible. In fact, the standard error of the fitted decay length was extremely large as λ_{W} = 186 ± 193 mm with x_{w} = −0.03 ± 0.20 mm. Therefore, the axial profile is dominantly determined by the geometrical effect.

This situation of course depends on the plasma parameters. Although T_{e} and n_{e} are not high (4 eV and 10^{18} m^{-3}) in this study, the decay due to the ionization should be visible in higher temperature and higher density plasmas. The present study suggested that the geometric effect should be taken into account in the low-density and/or low-temperature cases, because it can become a main process to determine the axial emission profile.

In summary, the sputtered W under He-Ar mixture plasma in NAGDIS-II was studied using a hyperspectral imaging camera. For eliminating the line integral effect, a small W disc was employed as the sputtering source and the Abel transform was applied. The axial profile of the local emission does not show simple exponential decay, and it was found that the effect of the particles spreading due to the geometric effect was dominant to determine the profile. This finding is useful for interpreting co-deposition experiments in linear plasma devices. The large geometric effect is mainly attributed to the use of a point W source. Thus, a flatter axial profile would be obtained by using a larger target. Even in such a case, however, the decay length cannot be easily obtained because the plasma profile on the target plane and the emitting angle dependence of sputtered particles must be taken into account in addition to the ionization.

The obtained results suggest that it is difficult to investigate the ionization decay length using small plasma devices. If the electron temperature were to increase tenfold to 40 eV, the ionization decay length would be reduced to about one-tenth. If the electron density were to increase tenfold or hundredfold, the decay length would also be reduced to one-tenth or one-hundredth, respectively. In the superconducting linear device Magnum-PSI, the plasma generated can have a electron density of $10^{20} - 10^{21}$ m^{-3}, which is the relevant to the ITER divertor condition [28]. In such a case, the ionization effect could be seen even with a similar setup.

The authors thank Mr. R. Chauhan from Eindhoven University of Technology and Mr. H. Yamamoto from Nagoya University for performing experiments. This research was supported by NIFS Collaboration Research program (NIFS22HDAF009).

[1] Y. Homma *et al.*, Nucl. Mater. Energy **12**, 323 (2017).
[2] T. Abrams *et al.*, Mater. Res. Express **10**, 126503 (2023).
[3] M. Kaufmann and R. Neu, Fusion Eng. Des. **82**, 521 (2007).
[4] V. Philipps, J. Nucl. Mater. **415**, S2 (2011).
[5] R. Causey *et al.*, J. Nucl. Mater. **266-269**, 467 (1999).
[6] J. Wesson and D.J. Campbell, *Tokamaks*, (Oxford university press, 2011), 149.
[7] T. Nakano, J. Nucl. Mater. **415**, S327 (2011).
[8] D. Nishijima *et al.*, J. Nucl. Mater. **415**, S96 (2011).
[9] S. Takamura *et al.*, Nucl. Fusion **52**, 123001 (2012).
[10] S. Kajita *et al.*, J. Appl. Phys. **132**, 181101 (2022).
[11] J. Coenen *et al.*, J. Nucl. Mater. **463**, 78 (2015).
[12] S. Kajita *et al.*, Nucl. Fusion **49**, 032002 (2009).
[13] S. Kajita *et al.*, Nucl. Mater. Energy **25**, 100828 (2020).
[14] A. Kirschner *et al.*, Plasma Phys. Control. Fusion **60**, 014041 (2017).
[15] N. Fedorczak *et al.*, J. Nucl. Mater. **463**, 85 (2015).
[16] C. Johnson *et al.*, Nucl. Fusion **63**, 096017 (2023).
[17] S. Kajita *et al.*, J. Nucl. Mater. **548**, 152844 (2021).
[18] S. Kajita *et al.*, Sci. Rep. **8**, 56 (2018).
[19] S. Kajita *et al.*, J. Nucl. Mater. **540**, 152350 (2020).
[20] M. Patino *et al.*, Nucl. Fusion **64**, 016011 (2023).
[21] N. Ohno *et al.*, Nucl. Fusion **41**, 1055 (2001).
[22] K. Dere, Astron. Astrophys. **466**, 771 (2007).
[23] W. Eckstein, IPP-Report, IPP 9/132 (2002).
[24] D. Nishijima *et al.*, Rev. Sci. Instrum. **91**, 083501 (2020).
[25] E. Marenkov *et al.*, J. Nucl. Mater. **496**, 18 (2017).
[26] S. Kajita *et al.*, J. Nucl. Mater. **420**, 252 (2012).
[27] OPEN-ADAS Project, OPEN-ADAS: Atomic Data and Analysis Structure for Fusion http://open.adas.ac.uk (2024).
[28] H. van Eck *et al.*, Fusion Eng. Des. **142**, 26 (2019).